Precision measurements of g_1 of the proton and of the deuteron with 6 GeV electrons

Y. Prok,[1,2,*] P. Bosted,[3,2] N. Kvaltine,[4] K. P. Adhikari,[1] D. Adikaram,[1] M. Aghasyan,[5] M. J. Amaryan,[1] M. D. Anderson,[6] S. Anefalos Pereira,[7] H. Avakian,[2] H. Baghdasaryan,[4] J. Ball,[8] N. A. Baltzell,[9,10] M. Battaglieri,[11] A. S. Biselli,[12] J. Bono,[13] W. J. Briscoe,[14] J. Brock,[2] W. K. Brooks,[15,2] S. Bültmann,[1] V. D. Burkert,[2] C. Carlin,[2] D. S. Carman,[2] A. Celentano,[11] S. Chandavar,[16] L. Colaneri,[17,18] P. L. Cole,[19] M. Contalbrigo,[5] O. Cortes,[19] D. Crabb,[4] V. Crede,[20] A. D'Angelo,[17,18] N. Dashyan,[21] R. De Vita,[11] E. De Sanctis,[7] A. Deur,[2] C. Djalali,[10] G. E. Dodge,[1] D. Doughty,[22,2] R. Dupre,[23,9] A. El Alaoui,[9,†] L. El Fassi,[9,‡] L. Elouadrhiri,[2] G. Fedotov,[10,24] S. Fegan,[11] R. Fersch,[3,§] J. A. Fleming,[25] T. A. Forest,[19] M. Garçon,[8] B. Garillon,[23] N. Gevorgyan,[21] Y. Ghandilyan,[21] G. P. Gilfoyle,[26] F. X. Girod,[2] K. L. Giovanetti,[27] J. T. Goetz,[16] W. Gohn,[28,‖] R. W. Gothe,[10] K. A. Griffioen,[3] B. Guegan,[23] N. Guler,[1,¶] K. Hafidi,[9] C. Hanretty,[4,#] N. Harrison,[28] M. Hattawy,[23] K. Hicks,[16] D. Ho,[29] M. Holtrop,[30] Y. Ilieva,[10,14] D. G. Ireland,[6] B. S. Ishkhanov,[24] E. L. Isupov,[24] S. Jawalkar,[3] X. Jiang,[31] H. S. Jo,[23] K. Joo,[28] N. Kalantarians,[4] C. Keith,[2] D. Keller,[4,16] M. Khandaker,[19,32] A. Kim,[33] W. Kim,[33] A. Klein,[1] F. J. Klein,[34] S. Koirala,[1] V. Kubarovsky,[2,35] S. E. Kuhn,[1] S. V. Kuleshov,[15,36] P. Lenisa,[5] K. Livingston,[6] H. Y. Lu,[10] I. J. D. MacGregor,[6] N. Markov,[28] M. Mayer,[1] B. McKinnon,[6] D. Meekins,[2] T. Mineeva,[28] M. Mirazita,[7] V. Mokeev,[2,24] R. A. Montgomery,[7,**] H. Moutarde,[8] A Movsisyan,[5] E. Munevar,[2] C. Munoz Camacho,[23] P. Nadel-Turonski,[2] S. Niccolai,[23] G. Niculescu,[27] I. Niculescu,[27] M. Osipenko,[11] A. I. Ostrovidov,[20] L. L. Pappalardo,[5] R. Paremuzyan,[21,††] K. Park,[2,10] P. Peng,[4] J. J. Phillips,[6] J. Pierce,[2] S. Pisano,[7,23] O. Pogorelko,[36] S. Pozdniakov,[36] J. W. Price,[37] S. Procureur,[8] D. Protopopescu,[6] A. J. R. Puckett,[28] B. A. Raue,[13,2] D. Rimal,[13] M. Ripani,[11] A. Rizzo,[17,18] G. Rosner,[6] P. Rossi,[7,2] P. Roy,[20] F. Sabatié,[8] M. S. Saini,[20] C. Salgado,[32] D. Schott,[14,13] R. A. Schumacher,[29] E. Seder,[28] Y. G. Sharabian,[2] A. Simonyan,[21] C. Smith,[2] G. Smith,[6] D. I. Sober,[34] D. Sokhan,[23] S. S. Stepanyan,[33] S. Stepanyan,[2] I. I. Strakovsky,[14] S. Strauch,[10] V. Sytnik,[15] M. Taiuti,[11] W. Tang,[16] S. Tkachenko,[4] M. Ungaro,[2,28] B. Vernarsky,[29] A. V. Vlassov,[36] H. Voskanyan,[21] E. Voutier,[38] N. K. Walford,[34] D. P. Watts,[25] L. B. Weinstein,[1] N. Zachariou,[10] L. Zana,[25,30] J. Zhang,[2] B. Zhao,[3] Z. W. Zhao,[4] and I. Zonta[17,18]

(CLAS Collaboration)

[1]*Old Dominion University, Norfolk, Virginia 23529, USA*
[2]*Thomas Jefferson National Accelerator Facility, Newport News, Virginia 23606, USA*
[3]*College of William and Mary, Williamsburg, Virginia 23187-8795, USA*
[4]*University of Virginia, Charlottesville, Virginia 22901, USA*
[5]*INFN, Sezione di Ferrara, I-44100 Ferrara, Italy*
[6]*University of Glasgow, Glasgow G12 8QQ, United Kingdom*
[7]*INFN, Laboratori Nazionali di Frascati, I-00044 Frascati, Italy*
[8]*CEA, Centre de Saclay, Irfu/Service de Physique Nucléaire, F-91191 Gif-sur-Yvette, France*
[9]*Argonne National Laboratory, Argonne, Illinois 60439, USA*
[10]*University of South Carolina, Columbia, South Carolina 29208, USA*
[11]*INFN, Sezione di Genova, I-16146 Genova, Italy*
[12]*Fairfield University, Fairfield Connecticut 06824, USA*
[13]*Florida International University, Miami, Florida 33199, USA*
[14]*The George Washington University, Washington, DC 20052, USA*
[15]*Universidad Técnica Federico Santa María, Casilla 110-V Valparaíso, Chile*
[16]*Ohio University, Athens, Ohio 45701, USA*
[17]*INFN, Sezione di Roma Tor Vergata, I-00133 Rome, Italy*
[18]*Universita' di Roma Tor Vergata, I-00133 Rome, Italy*
[19]*Idaho State University, Pocatello, Idaho 83209, USA*
[20]*Florida State University, Tallahassee, Florida 32306, USA*
[21]*Yerevan Physics Institute, 375036 Yerevan, Armenia*
[22]*Christopher Newport University, Newport News, Virginia 23606, USA*
[23]*Institut de Physique Nucléaire ORSAY, Orsay, France*
[24]*Skobeltsyn Institute of Nuclear Physics, Lomonosov Moscow State University, 119234 Moscow, Russia*
[25]*Edinburgh University, Edinburgh EH9 3JZ, United Kingdom*
[26]*University of Richmond, Richmond, Virginia 23173, USA*
[27]*James Madison University, Harrisonburg, Virginia 22807, USA*
[28]*University of Connecticut, Storrs, Connecticut 06269, USA*
[29]*Carnegie Mellon University, Pittsburgh, Pennsylvania 15213, USA*
[30]*University of New Hampshire, Durham, New Hampshire 03824-3568, USA*
[31]*Los Alamos National Laboratory, Los Alamos, New Mexico 87545, USA*
[32]*Norfolk State University, Norfolk, Virginia 23504, USA*
[33]*Kyungpook National University, Daegu 702-701, Republic of Korea*
[34]*Catholic University of America, Washington, D.C. 20064, USA*
[35]*Rensselaer Polytechnic Institute, Troy, New York 12180-3590, USA*

[36]*Institute of Theoretical and Experimental Physics, Moscow, 117259, Russia*
[37]*California State University, Dominguez Hills, Carson, California 90747, USA*
[38]*LPSC, Université Grenoble-Alpes, CNRS/IN2P3, INPG, Grenoble, France*
(Received 1 May 2014; published 29 August 2014)

The inclusive polarized structure functions of the proton and deuteron, g_1^p and g_1^d, were measured with high statistical precision using polarized 6 GeV electrons incident on a polarized ammonia target in Hall B at Jefferson Laboratory. Electrons scattered at laboratory angles between 18 and 45 degrees were detected using the CEBAF Large Acceptance Spectrometer (CLAS). For the usual deep inelastic region kinematics, $Q^2 > 1$ GeV^2 and the final-state invariant mass $W > 2$ GeV, the ratio of polarized to unpolarized structure functions g_1/F_1 is found to be nearly independent of Q^2 at fixed x. Significant resonant structure is apparent at values of W up to 2.3 GeV. In the framework of perturbative quantum chromodynamics, the high-W results can be used to better constrain the polarization of quarks and gluons in the nucleon, as well as high-twist contributions.

DOI: 10.1103/PhysRevC.90.025212 PACS number(s): 14.20.Dh, 13.60.Hb, 13.88.+e, 27.10.+h

I. INTRODUCTION

A full understanding of the spin structure of the nucleon, including the determination of the polarized gluon density $\Delta G(x)$ in particular, is a major goal of hadronic physics. Deep-inelastic lepton scattering from nucleons has proved over the years to be the cleanest tool to study the short-distance structure of the nucleon. The pioneering experiments at SLAC, followed by several generations of experiments at FermiLab, SLAC, CERN, DESY, and elsewhere, have made great strides in determining the spin-averaged parton densities of the quarks and gluons in the proton and neutron. Starting in the 1970s, experiments using polarized targets have been making steady progress in determining the spin-dependent longitudinal parton densities, although over a more restricted range in momentum fraction x and momentum transfer squared Q^2 because of the lower luminosity available with polarized targets. See Ref. [1] for a recent review. Initial studies from SLAC and CERN, borne out with increased precision by subsequent experiments at SLAC-[2,3], CERN-[4], DESY-[5], and JLab [1,6], showed that the up and down quarks sum to only a small fraction of total spin of the nucleon in the framework of perturbative quantum chromodynamics (QCD). This implied that the net contribution of polarized gluons, strange quarks, and parton angular momentum must be substantial. A large effort is ongoing to study these contributions.

For gluon spin, two approaches are being followed. The first is to try to isolate specific processes in which a polarized gluon is involved at leading order, for example, photon-gluon fusion leading to a pair of charmed quarks (COMPASS) [4], or quark-gluon scattering leading to a high energy photon (RHIC spin) [7]. The interpretation of these interactions is complicated both because of background events (other tree-level processes that can lead to the same final state) and higher order QCD corrections [1].

The second approach examines the Q^2 dependence of the spin structure function g_1. Perturbative QCD allows a simple expression of g_1 in terms of the quark, antiquark, and gluon distributions Δq, $\Delta\overline{q}$, and ΔG, which evolve in leading order according to the DGLAP equations [8]:

$$g_1(x,Q^2)_{\text{pQCD}} = \frac{1}{2}\sum e_q^2\Big[(\Delta q + \Delta\overline{q}) \otimes \left(1 + \frac{\alpha_s(Q^2)}{2\pi}\delta C_q\right) + \frac{\alpha_s(Q^2)}{2\pi}\Delta G \otimes \frac{\delta C_G}{N_f}\Big], \quad (1)$$

where α_s is the strong coupling factor, δC_q and δC_G are the Wilson coefficients, N_f is the number of quark flavors, and $\otimes$ indicates a convolution integral.

In the spin-averaged case, pQCD evolution is the benchmark approach to which reaction-specific determinations of the gluon density, $G(x)$, are compared. This is possible because of the high precision of measurements of the spin-averaged structure function F_2 over many decades in both x and Q^2 (needed because the logarithmic evolution due to gluon radiation is very slow). In the polarized case, the kinematic range of present precision data is considerably more limited. Nonetheless, the data are of sufficient quality to obtain a very good description of the valence up and down quark densities, and rough indications of the gluon and sea quark densities [1].

In practice, fits to data should include the effects of both kinematic and dynamic higher twist, especially in the pre-asymptotic regime of this experiment. We can decompose $g_1(x,Q^2)$ into leading twist and higher twist components [9] :

$$g_1(x,Q^2) = g_1(x,Q^2)_{\text{LT}} + g_1(x,Q^2)_{\text{HT}}. \quad (2)$$

*Corresponding author: yprok@jlab.org
†Current address: Universidad Técnica Federico Santa María, Casilla 110-V Valparaíso, Chile.
‡Current address: Old Dominion University, Norfolk, Virginia 23529, USA.
§Current address: Christopher Newport University, Newport News, Virginia 23606, USA.
‖Current address: University of Kentucky, Lexington, KY 40506, USA.
¶Current address: Los Alamos National Laboratory, Los Alamos, NM 87544, USA.
#Current address: Thomas Jefferson National Accelerator Facility, Newport News, Virginia 23606, USA.
**Current address: University of Glasgow, Glasgow G12 8QQ, United Kingdom.
††Current address: Institut de Physique Nucléaire ORSAY, Orsay, France.

The leading twist term can be expressed as a sum of the well-known pQCD term $g_1(x,Q^2)_{\rm pQCD}$ [1], the calculable kinematic target mass corrections, and higher order terms:

$$g_1(x,Q^2)_{\rm LT} = g_1(x,Q^2)_{\rm pQCD} + h^{\rm TMC}(x,Q^2)/Q^2 + \mathcal{O}(1/Q^4). \quad (3)$$

The dynamic higher twist contribution represents the parton-parton correlations in the target nucleon and is given by

$$g_1(x,Q^2)_{\rm HT} = h(x,Q^2)/Q^2 + \mathcal{O}(1/Q^4). \quad (4)$$

The dynamic higher twist corrections are nonperturbative in nature and cannot presently be calculated in a model-independent way. However, they can be extracted directly from the experimental data, which was done recently with CLAS and COMPASS data by the LSS group [9], and with CLAS, COMPASS, HERMES, and CERN data by the JAM collaboration at Jefferson Lab [10].

The goal of the present experiment is to provide much higher statistical precision in measurements of g_1^p and g_1^d than was previously available in the kinematic range accessible with 6 GeV electrons at Jefferson Lab. This precision is needed to distinguish between power-law higher twist and logarithmic gluon radiation in the polarized parton densities in the nucleon. Much of the present data also lie in the pre-asymptotic region, and exhibit significant resonance structure, which needs to be taken into account by QCD fits including the higher twist terms. These data will be particularly valuable when combined with planned data with 11 GeV electrons.

II. THE EXPERIMENT

A. Experimental context

This experiment was carried out at Jefferson Lab, using longitudinally polarized electrons incident on longitudinally polarized protons and deuterons in solid ammonia targets, and the CEBAF Large Acceptance Spectrometer (CLAS) [11]. Data from several previous experiments with solid polarized targets have been analyzed and published [6,12], and some are still in the analysis stage.

The present experiment used 6 GeV electrons and relatively larger scattering angles to focus on the deep inelastic region (DIS). The main focus of this experiment was on semi-inclusive DIS (SIDIS) and deeply virtual Compton scattering (DVCS), both of which required the detection of photons at small angles. For this reason, an inner calorimeter (IC) was installed, which blocked scattered electrons below about 18 degrees. The IC is not used in the present inclusive analysis.

The present analysis closely follows those of its predecessors [6,12]. Small differences arise from the use of $^{14}NH_3$ instead of $^{15}NH_3$, a 50% longer target cell, the inclusion of the IC detector into CLAS, and an improved treatment of the effects of the polarized target magnetic field.

B. Experimental overview

The experiment, named "eg1-dvcs," used 6 GeV longitudinally polarized electrons from CEBAF at Jefferson Lab impinging on a longitudinally polarized solid ammonia target of 0.025 radiation length, immersed in liquid helium [13]. Inclusive scattered electrons were detected in CLAS [11]. The typical beam current was 7 nA, which, when integrated over the 6 months of data taking, resulted in approximately 2×10^{17} electrons traversing the target. The beam polarization, as periodically measured using Møller scattering in an upstream polarimeter, averaged 85% for the first three quarters of the experiment. A lower polarization of about 75% was delivered during the remaining time.

About 70% of the running time was on polarized protons (NH_3 target), 20% on polarized deuterons (ND_3 target), 10% on a reference unpolarized carbon target, and 1% on an empty cell. The 1.5-cm-diameter cells typically contained 1 g/cm^2 of material immersed in a 2-cm-long liquid helium bath. The target insert housed two such cells, which were called the "top," and the "bottom" cells. The target polarization, monitored by an NMR system, averaged between 75% and 90% for the proton target, and between 25% and 40% for the deuteron target. The average dilution factor, defined as the ratio of events from polarized protons or deuterons in the NH_3 or ND_3 target to the total number of events, was 0.16–0.19 for the NH_3 target and 0.21–0.23 for the ND_3 target.

To minimize loss of polarization from beam heating, the sub-millimeter-diameter beam was uniformly rastered over the front face of the target with a period of a few seconds. The beam position, averaged over a few minutes or longer, was kept stable at the 0.1-mm level, using feedback from a set of beam position monitors. A split solenoid superconducting magnet provided a highly uniform 5-T magnetic field near the target, which effectively extended about 20 cm up- and downstream from the target center.

Scattered electrons were detected in the CLAS detector [11] in Hall B, over the polar angle range of about 18–48 degrees. A typical event in CLAS is shown in Fig. 1.

The CLAS, comprised of six azimuthally symmetric detector arrays, uses a toroidal field to bend charged particles. Particle momenta and scattering angles were measured with a drift chamber (DC) tracking system with a relative accuracy of 0.3%–2% in momentum, and about 3 mr in angle. Electrons were separated from a significantly larger flux of charged pions using segmented gas Cherenkov detectors (pion threshold 2.6 GeV) and an electromagnetic calorimeter. A hardware trigger system made the first selection, rejecting about 90% of pions while keeping close to 99% of electrons, to not overwhelm the data acquisition system. The hardware Cherenkov and calorimeter thresholds were adjusted to give a trigger rate of about 3000 Hz, and a "dead time" in which no trigger could be accepted of about 10%. An additional unbiased trigger was prescaled by a large factor to measure the efficiency of the main electron trigger.

The data taking was divided into three parts: Part A in early 2009 used NH_3 as the target, centered at 58 cm upstream of CLAS center ($z_0 = -58$ cm); Part B (mid-2009) also used NH_3, this time at $z_0 = -68$ cm; and Part C (September 2009) mostly used ND_3 as the target, again with $z_0 = -68$ cm. Each part had slightly different primary beam energies (between 5.7 and 6.0 GeV, with several days at 4.8 GeV at the end of Part A). The CLAS torus polarity was set to bend electrons inwards for almost all of Parts A and B, and about two-thirds of Part C. The field strength was two-thirds of the maximum

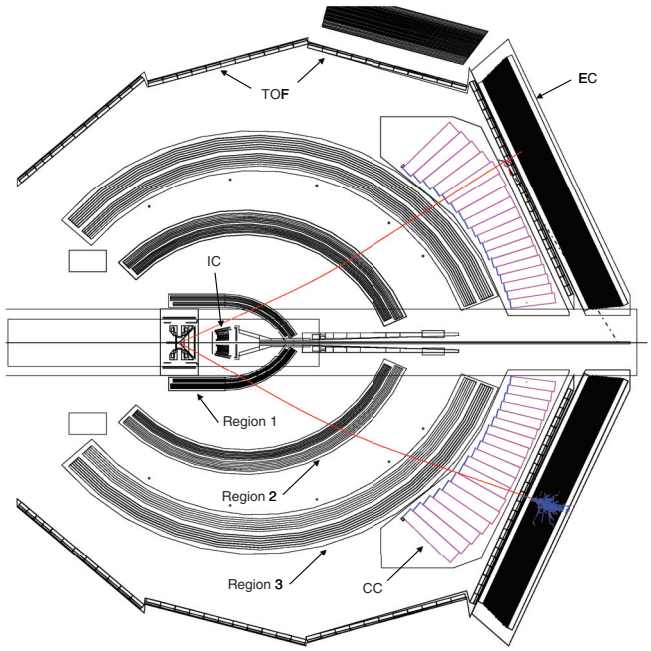

FIG. 1. (Color online) A schematic of an event in CLAS, with two charged particles passing through three regions of drift chambers (DC), the time of flight (TOF, also known as SC), the Cherenkov counters (CC), and the electromagnetic calorimeter (EC).

available (2250 A), resulting in better acceptance for low momentum charged particles, but somewhat worse momentum resolution.

III. DATA ANALYSIS

For the present analysis, the only particles of interest were scattered electrons. The spin structure functions were determined from the difference in rates in a particular x and Q^2 bin for beam and target polarizations aligned or antialigned. A large background of scattering from unpolarized (or slightly polarized) material in the target was taken into account using a detailed model of the target composition, combined with a fit to world cross-section data.

A. Data processing

The raw data consisted of approximately 50 000 files, each about 2 GB in size and corresponding to a few minutes of data taking. The files were grouped into runs consisting of about 80 files, on average, all with the same experimental configuration. Each file was processed with the standard CLAS analysis package [14].

The processed data were corrected using an improved method of tracking particles through the target magnetic field. The standard method in the CLAS reconstruction package swims particles backwards to a plane perpendicular to the appropriate sector. A more accurate method is to swim back to the x and y coordinates specified by the raster magnet. This method used the track coordinates at the first layer of Drift Chambers and a fit to a large ensemble of simulated forward-swimming particles. This ensured that the track would intersect the beam line for a given raster magnet setting. The net result was about a factor of two improved angular resolution, as verified by the width of the beam energy E_0, reconstructed from the electron and proton scattering angles in ep elastic scattering.

B. Calibrations

1. Standard calibrations

Standard calibration procedures were done for each of the subsystems in CLAS. These included drift chamber (DC) alignment using straight-through tracks; DC timing alignments; gas Cherenkov detector (CC) pulse height alignment using single photoelectron peaks; time-of-flight scintillator (SC) timing corrections; and electromagnetic calorimeter (EC) pulse height corrections using cosmic rays. Timing and position resolutions for each of the systems, after calibration, were similar to those obtained during other electron running periods [11]. Calibrations were made frequently enough to ensure very good stability for these detector systems.

2. Raster corrections

An additional calibration specific to experiments with polarized targets was done. This was to calibrate the beam position at the target, which depended on steering in the accelerator, as well as the strength of the magnetic field used to raster the beam. The x and y magnet field (in units of ADC counts) was recorded for each event trigger. By minimizing the width of the reconstructed target position along the beam line (z), the relation between magnet current and beam position was determined, as well as the beam position relative to the CLAS center for no raster magnetic field. The fit also determined the target center along the beam line relative to the center of CLAS: -57.95 cm for Part A, and -67.95 cm for parts B and C of the run.

3. Magnet angle correction

Another calibration specific to this experiment was the determination of the orientation of the target solenoid with respect to the beam line. The primary method used was to make the opening angle of reconstructed electron-positron pairs (from photon conversions) as close to zero as possible, independent of the azimuthal angle of the pair relative to the beam line axis. The result of the study was an approximately 3-mr tilt, resulting in a significant polar deflection of charged particles, on top of the azimuthal rotation characteristic of a solenoidal field. An analysis using the overconstrained kinematics of exclusive ep elastic scattering confirmed the 3-mr tilt.

C. Event selection

In this experiment, the events of interest are those with at least one well-identified electron originating from the target. The two detectors used for particle ID were the threshold gas Cherenkov detector (CC, pion threshold of 2.6 GeV) and the lead-scintillator electromagnetic calorimeter (EC), with a nominal sampling fraction of 0.30. The first level of selection was in the electronic trigger, which required about

1 photoelectron (p.e.) in the CC and an energy deposition of 0.5 GeV in the EC. In software, an electron was identified by first requiring that a time-based drift-chamber (DC) track have negative charge, use at least five of the six superlayers in the tracking system, and have a signal in each of the CC, EC, and scintillator time-of-flight counter system (SC). A further requirement was that the CLAS sector number for each of the subsystems (DC, CC, SC, and EC) be matched. We then required eight additional particle ID cuts:

(1) The number of photoelectrons (p.e.) in the CC must be greater than 2 p.e.
(2) The energy in the EC divided by momentum P (with 0.12 GeV offset) must be greater than $0.80(E/P)_{\text{peak}}$, where $(E/P)_{\text{peak}}$ is the peak of the $E/(P-0.12)$ distribution (from a first pass through the data), averaged over each run, for each sector separately. This procedure was performed to take out slow drifts in the EC gain, which were especially evident in rare cases when the high voltage on the PMTs had been off for a significant period of time. The offset of 0.12 GeV was obtained from a fit to data with $1.2 < P < 5$ GeV, and can be attributed to the energy losses in the detectors in front of the EC, as well as the minimum ADC signal size used in this analysis. The distribution of EC energy divided by momentum P (with 0.12 GeV offset) plotted vs the number of photoelectrons in the Cherenkov detector can be seen in Fig. 2.
(3) The target vertex position along the beam line (z) must be within 3 cm of the polarized target center.
(4) The difference $\delta\phi_{\text{DC1}}$ between the electron's polar angle at the first drift chamber layer and the azimuthal component of its momentum at the same location must be zero within $\pm 4^\circ$. Particles with higher $\delta\phi_{\text{DC1}}$ are more likely to have scattered from materials that were not part of the target and so can have inaccurate kinematics.
(5) The Cherenkov mirror number must be aligned with the value expected from the track trajectory (as defined by the nearby SC paddle number) within two SC paddles. This method uses the feature that the SC paddles and CC mirrors are close together so that their correlation is relatively insensitive to the track trajectories.
(6) The Cherenkov signal time must agree with the EC signal time within ± 4 ns.
(7) The electron scattering angle θ_e must be less than 40 degrees for Part A, and less than 45 degrees for parts B and C, to eliminate large angle particles that could have passed through the significant amounts of the heat shield and superinsulation in the target.
(8) The electrons' trajectories must not pass too close to the lead shielding around the IC (or the IC support stand). The reason for this cut is that electrons passing through short lengths of the shielding could survive, but with strongly modified angles and momenta from multiple scattering and Bremsstrahlung, thus resulting in an incorrect determination of their original kinematic values.

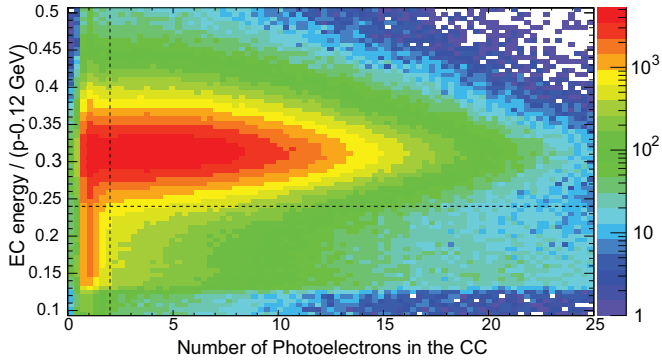

FIG. 2. (Color online) Distribution of electron candidates in the EC energy divided by momentum P (with 0.12 GeV offset) plotted vs the number of photoelectrons in the Cherenkov detector. The dashed lines show the cuts applied.

D. Quality checks

1. Beam scraping

Careful on-line monitoring ensured that very few data were taken with the beam scraping on the relatively thick and unpolarized target side walls. An off-line check revealed a few files with this problem, which were removed from further analysis.

2. Rate stability

To avoid significant corrections to the measured asymmetries, and also to obtain reliable dilution factors from the comparison of ammonia and carbon target rates, we removed data files where an obvious drop in efficiency occurred. The most common reasons for the loss of efficiency were that parts of the DC or EC tripped off.

3. Asymmetry stability

The study of the average inclusive electron double-spin asymmetry proved to be a very valuable quality check. This asymmetry is zero for carbon targets, and generally at least 3-sigma difference from zero for polarized target runs. The sign of the asymmetry indicated whether the overall beam and target polarized signs were correct in the database. Figure 3 shows the final results for the double spin asymmetry as a function of run number. In Part C, the NH_3 and ND_3 targets could also be distinguished due to the much smaller asymmetries for ND_3 compared to NH_3. After all corrections, the polarized target runs all show a positive asymmetry, while the carbon runs are all consistent with zero.

4. Electron detection efficiency

The electron detection efficiency was determined by comparing the rates from the carbon target to those expected, based on fits to world data [15]. Radiative effects and pair-symmetric backgrounds were taken into account. The typical efficiency was ~75%, except for Sector 5, where it was only ~40%, due to a leak in the Cherenkov detector. The efficiency was found to decrease with increasing beam current, at a relative rate of about 1%/nA. This decrease is attributed to higher

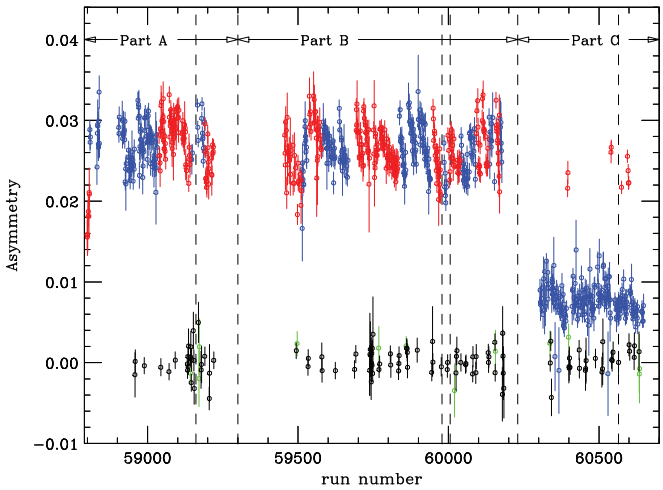

FIG. 3. (Color online) Average raw double-spin count asymmetries vs run number. The black points are for carbon, the green points for the empty cell, the red points for the bottom NH_3 target, and the blue points for the top NH_3 target (Parts A and B) or the ND_3 target (Part C). The vertical dashed lines correspond to changes in beam energy or torus polarity.

drift-chamber occupancy at higher beam current, resulting in lower tracking efficiency.

5. *Beam energy*

The beam energy was determined using measurements from the other two experimental halls at JLab, which accurately measure the deflection of the beam in dipole magnets. These results were confirmed using the overconstrained kinematics of exclusive ep elastic scattering. The results are $E_0 = 5.887$, $E_0 = 5.954$, and $E_0 = 5.752$ GeV for Parts A, B, and C, respectively. The estimated uncertainty is 5 MeV.

E. Double-spin asymmetries

The double-spin asymmetry $A_\parallel$ was formed in each two-dimensional physics bin using

$$A_\parallel^p = \frac{N^{\uparrow\Downarrow} - N^{\uparrow\Uparrow} r_c}{N^{\uparrow\Downarrow} + N^{\uparrow\Uparrow} r_c} \frac{c_s}{f\ (1+c_1)\ P_b\ P_t\ f_{\rm RC}} + A_{\rm RC}, \quad (5)$$

for NH_3 and

$$A_\parallel^d = \left(\frac{N^{\uparrow\Downarrow} - N^{\uparrow\Uparrow} r_c}{N^{\uparrow\Downarrow} + N^{\uparrow\Uparrow} r_c} \frac{c_s}{f\ (1+c_1)\ P_b\ P_t} - c_2 A_\parallel^p \frac{\sigma_p}{\sigma_d} \right) \times \frac{1}{f_{\rm RC}} + A_{\rm RC}, \quad (6)$$

for ND_3, where $N^{\uparrow\Uparrow}$ ($N^{\uparrow\Downarrow}$) are the number of counts in the parallel (antiparallel) beam helicity bins, r_c is the ratio of incident beam charges for the two helicities, f is the bin-averaged dilution factor, defined as the ratio of events from polarized protons or deuterons in the NH_3 or ND_3 target to the total number of events, c_s is the pair-symmetric correction, c_1 accounts for polarized nitrogen in the NH_3 and ND_3 targets, c_2 accounts for the polarized NH_3 mixed into the ND_3 target, P_b is the beam polarization, P_t is the target polarization, $A_\parallel^p$ is the measured value of the proton asymmetry, $A_\parallel^d$ is the deuteron asymmetry, $f_{\rm RC}$ is a radiative dilution factor, and $A_{\rm RC}$ is an additive radiative correction. Each of the factors in Eqs. (5) and (6) is discussed below. Numerical values can be found in the tables of final results in the Appendix of the *arxiv* version of this paper, and are also stored in the CLAS Physics Database [16].

F. Raw asymmetry

Data processing consisted of determining the number of electron events passing the particle ID cuts mentioned above, for each run, in bins of momentum P, polar scattering angle θ, and helicity (beam and target polarizations either aligned or antialigned). The main reason for choosing bins in (P,θ) at the data processing stage, was to allow flexibility later on to slightly vary the beam energy E_0 from the nominal value.

Counts were summed for each target and each run period: Part A, 5.9 GeV; Part B, in-bending; Part B, out-bending; Part C, in-bending; and Part C, out-bending.

The bin sizes were 0.04 GeV in momentum and 0.2 degree in θ, chosen to be small enough to allow redistribution into physics bins of (x, Q^2) and (W, Q^2),

$$W = \sqrt{M^2 + 2M\nu - Q^2}, \quad (7)$$

where W is the invariant mass of the final state.

Here, ν is the virtual photon energy, equal to the difference in the incident and scattered electron energies: $\nu = E_0 - E'$,

$$Q^2 = -q^2 = 4E_0 E' \sin^2 \frac{\theta}{2} \quad (8)$$

is the four-momentum transfer, and

$$x = \frac{Q^2}{2M\nu} \quad (9)$$

is the Bjorken scaling variable. During the redistribution process, the average values of all relevant physics quantities were calculated.

G. Correction factor r_c

The ratio of incident charges for the two beam helicity states takes into account any difference in the integrated incident current for one state compared to the other. Because the beam helicity was reversed at 30 Hz, and came in alternating helicity buckets, the difference came about only due to helicity-dependent beam current differences, which were kept to less than 1 part in 1000 on a few minute scale by a feedback system, and less than 1 part in 10 000, averaged over a month-long time scale. Therefore, effectively $r_c = 1$.

H. Target and beam polarization

For this inclusive analysis, only the product of target polarization (P_t) and beam polarization (P_b) is important, but not the individual values. For the NH_3 targets, the individual measurements of each quantity (NMR for P_t and Møller scattering for P_b) had relative systematic uncertainties of over 4%. We therefore used ep elastic scattering, for which the uncertainty on the measured asymmetry is of order 1%

statistical and $< 2\%$ systematic. Another advantage is that the same runs were used as for the inclusive analysis, so any run-dependent biases would tend to cancel.

We selected electrons using similar particle ID cuts as those used for the inclusive analysis. We selected protons using a ± 0.7-ns cut on the difference in predicted and measured times between the electron and proton, determined with the SC system. The cuts used to select ep elastic events were

(1) The missing energy must be less than 120 MeV.
(2) The missing longitudinal (transverse) momentum relative to the incident beam direction must be less than 120 MeV (80 MeV).
(3) $|W - M| < 0.08$ GeV.
(4) The beam energy reconstructed from electron and proton scattering angles only must agree with the nominal beam energy to 70 MeV.

The last cut was especially powerful in reducing the background from quasielastic events from nitrogen and helium to about 3%. The dilution-corrected double-spin asymmetry was then formed for each of seven Q^2 bins, and $P_b P_t$ was extracted from the ratio to the theoretically well-known asymmetry for ep elastic scattering. The values were then averaged over Q^2, which ranged from about 2 to 7 GeV^2. No dependence on Q^2 was observed. The results are consistent with the product of the individual measurements of P_b and P_t.

For the ND_3 target, the kinematic region where there is the best sensitivity to ed quasielastic scattering was heavily contaminated by the polarization of the 10% NH_3 in the target. On the other hand, the direct deuteron polarization measurements using NMR are more accurate than for the proton, thanks to the "double peak" fitting method, which removes the sensitivity to the hard-to-measure thermal equilibrium signal [17].

We therefore used the count-weighted product of target polarization from NMR and beam polarization from Møller measurements. We estimated the systematic uncertainty of 3% in P_t and 4% in P_b.

Using these values as a constraint, we then fit the ep coincidence data in the region of small missing momentum to obtain $P_b P_t = 0.50$ for the protons in the ND_3 target. The results for all targets are given for each set of running conditions in Table I.

TABLE I. Average values of proton and deuteron $P_b P_t$ for all run periods. The results for Part C and NH_3 target are for the $\sim 11\%$ of NH_3 contaminating the ND_3 target.

Run period	Target	$P_b P_t$
Part A (5.9 GeV)	NH_3	0.637 ± 0.011
Part B (in-bending)	NH_3	0.645 ± 0.007
Part B (out-bending)	NH_3	0.579 ± 0.037
Part C (in-bending)	NH_3	0.50 ± 0.04
Part C (out-bending)	NH_3	0.51 ± 0.06
Part C (in-bending)	ND_3	0.216 ± 0.010
Part C (out-bending)	ND_3	0.236 ± 0.010

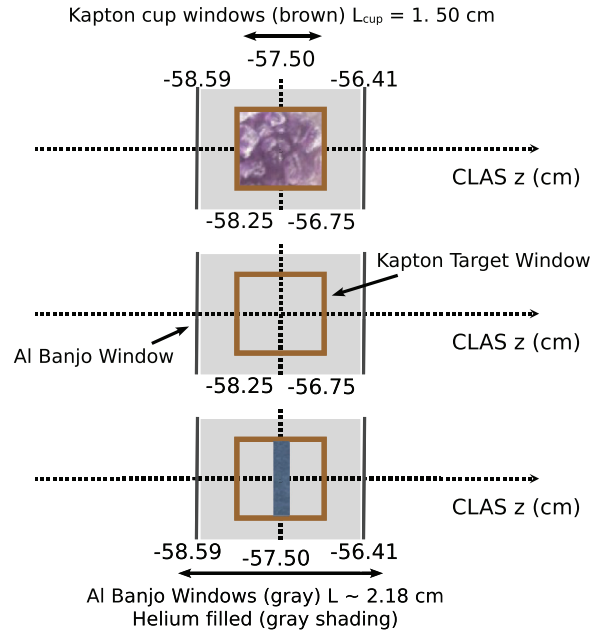

FIG. 4. (Color online) Schematic diagram for eg1-dvcs showing the targets used: loosely packed ammonia beads (top), an empty target cell (middle), and a solid carbon target (bottom). Ammonia was the primary experimental target used; carbon and empty targets were used to calculate dilution factors and to make consistency checks. Two ammonia cells were used during the experiment (one is not shown here).

I. Dilution factor

The dilution factor f is defined as the fraction of inclusive scattering events originating from polarized hydrogen or deuterium, as compared to the total number of scattering events from all materials in the target. The electron beam in our experiment passed through: helium (He), Kapton (K), ammonia ($^{14}NH_3/^{14}ND_3$), and aluminum (Al). A schematic diagram of the three target cells is shown in Fig. 4.

If we define n_{material} as the electron scattering rate from a particular target material, we can write for the proton,

$$f = \frac{n_p}{n_{NH_3} + n_{He} + n_{Al} + n_K}. \tag{10}$$

The event rate for each material i is proportional to the product of the areal density $\tilde{\rho}$ and the inclusive DIS cross section σ,

$$n_i \propto \tilde{\rho}_i \sigma_i \propto \rho_i l_i \sigma_i, \tag{11}$$

where ρ_i is the volume density and l_i is the length of each material. The constant of proportionality depends on detector acceptance, but because the target materials do not change with time, this constant is the same for the numerator and denominator, and it cancels out of the ratio. The dilution factor for the $^{14}NH_3$ target is then (we replace the symbol $^{14}NH_3$ by a symbol A),

$$\frac{\frac{3}{17}\rho_A l_A \sigma_A}{\rho_{He}(L - l_A)\sigma_{He} + (\frac{14}{17}\sigma_N + \frac{3}{17}\sigma_p)\rho_A l_A + \rho_{Al} l_{Al} \sigma_{Al} + \rho_K l_K \sigma_K}, \tag{12}$$

TABLE II. Average areal densities in units of g/cm^2 for each of the materials in the four targets of the experiment. Kapton is not mentioned here, but is approximated as pure carbon. The results correspond to $L = 2.0$ cm and $l_A = 0.87$ cm ($l_A = 0.89$ cm) for the NH_3 (ND_3) target.

Target	H	D	He	C	N	Al
NH_3	0.133	0	0.164	0.009	0.621	0.045
ND_3	0.015	0.239	0.161	0.009	0.628	0.045
Empty	0	0	0.290	0.009	0	0.045
Carbon	0	0	0.232	0.886	0	0.045

where L is the length of the He bath and l_A is the effective ammonia length. The radiated cross sections are a function of the length of the material in units of radiation length and are obtained by modeling the available world data, and the areal density for each material was measured in the laboratory or obtained from the literature. The average areal densities of each of the materials are listed in Table II.

As shown by Eq. (12), to accurately determine the dilution factor we need to know the total length of the He bath (L) in the target and the packing fraction or "length" (l_A) of the NH_3 beads in the target cup.

1. Length of the He bath (L)

The distance L between the aluminum windows that contain the liquid He was measured at room temperature to be 2.3 ± 0.3 cm. The large uncertainty arises because the windows are very thin and hence can bow inwards or outwards, depending on pressure differences. We therefore relied primarily on data taken with the empty target and no helium bath, where two peaks in the vertex-Z distribution could be clearly seen, corresponding to the windows. The peak separation from these measurements is 2.0 ± 0.1 cm.

A check was made by extracting L from measurements of the empty and carbon targets, with and without helium present, and assuming a helium density of 0.145 g/cm^2.The average value of L from a set of 10 such measurements was 2.1 ± 0.1 cm.

2. Ammonia length l_A (the packing fraction)

The other quantity extracted is the packing fraction of the ammonia beads in the Kapton target cup. This gives us the apparent length of the ammonia target as if it were packed into a solid piece as opposed to crushed beads.

The method used to determine l_A was to fit for the value that best described the measured ratios of electron rates from the carbon and ammonia targets. The predictions used fits to world data taking into account radiative effects using the Mo-Tsai formalism [26]. The dependence of external radiative corrections on l_A were taken into account in the fits. For each carbon target run, the run on ammonia closest in time was chosen to obtain a value of l_A to minimize the effects of slow drifts in average detection efficiency. A summary of the results is presented in Table III.

TABLE III. Effective ammonia lengths l_A for three run periods and two target cells.

Part	Target cup	Packing fraction l_A
Part A	Top	0.85 ± 0.03 cm
Part A	Bottom	0.85 ± 0.03 cm
Part B	Top	0.86 ± 0.03 cm
Part B	Bottom	0.91 ± 0.03 cm
Part C	Top	0.92 ± 0.03 cm
Part C	ND3	0.89 ± 0.025 cm

3. NH_3 contamination of the ND_3 target

The manufacturer's specification for the deuterium gas used to make the ammonia beads had <1% hydrogen contamination. A check was made using *ep* elastic data, and the actual contamination was, surprisingly, found to be an order of magnitude larger. After standard *ep* elastic exclusivity cuts, the events from hydrogen, deuterium, and heavier nuclei could clearly be distinguished by plotting the event rates as a function of missing transverse momentum p_T^q, relative to the momentum transfer vector $\vec{q}$. In the case of a free proton, the p_T^q distribution is a delta function widened by our experimental resolution. In the case of the deuteron, it is considerably wider due to the average 50-MeV Fermi motion of the proton in the deuteron. In the case of heavier nuclei such as carbon and nitrogen, the peak is another factor of four wider, because the typical Fermi momentum is on the order of 200 MeV. These features are illustrated in Fig. 5.

The distribution of p_T^q for the carbon target is very wide, and that for the NH_3 target has a very narrow peak, sitting on top of a wide distribution with the same shape as for the carbon target. The ND_3 target spectrum has the expected medium-width peak from free deuterons in the target, sitting on top of a nuclear background from nitrogen. Unfortunately, a very narrow peak of the same width as seen in the NH_3 target is also clearly visible. Using data from the carbon and NH_3 targets as a guide, we performed fits to the three components visible in the ND_3 spectra to obtain the relative fraction of free protons and deuterons. The result of the study was that $10.5 \pm 0.4\%$ of the ND_3 effective target length was NH_3, for

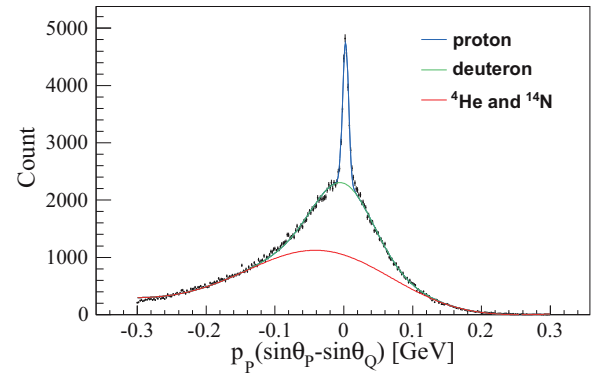

FIG. 5. (Color online) Distribution of p_T^q for exclusive *ep* elastic scattering from the deuterated ammonia (ND_3) target.

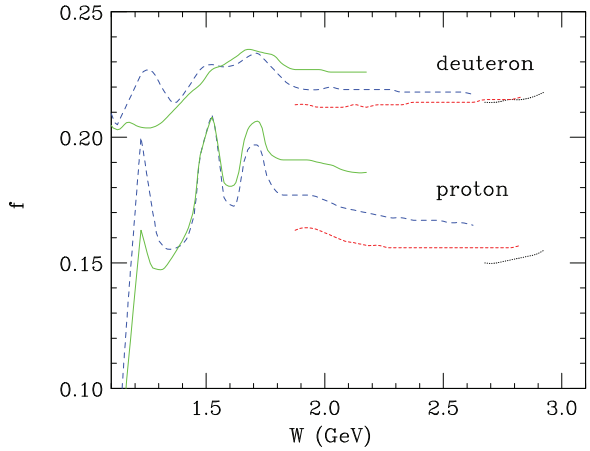

FIG. 6. (Color online) Dilution factor as a function of W for $Q^2 = 1$ GeV^2 (black, dotted curve), $Q^2 = 1.6$ GeV^2 (red, short-dash curve), $Q^2 = 3$ GeV^2 (blue, long-dash curve), and $Q^2 = 5$ GeV^2 (green, solid curve). The lower set of curves is for the ammonia (NH_3) target, while the upper set of curves is for the deuterated ammonia (ND_3) target.

the in-bending runs, and $12.0 \pm 0.7\%$ for the out-bending runs. No time dependence to the contamination was observed within each of these run periods.

4. Dilution factor results

Having determined the areal density of each component of each target, we used the method outlined above to calculate the corresponding dilution factor as a function of (x, Q^2) and (W, Q^2). The results for NH_3, using a typical value $l_A = 0.87$ cm, are shown in Fig. 6 as a function of W for four values of Q^2.

Clear resonance structure can be seen corresponding to the three well-established resonance regions near $W = 1.23$, 1.5, and 1.7 GeV, arising primarily from the W dependence of the ratio of proton to neutron cross sections. The dilution factor for the deuteron shows much weaker structure, because the deuteron and the $A > 2$ materials both contain almost equal numbers of proton and neutrons.

J. c_s correction

The c_s correction factor primarily takes into account the background contribution from electrons produced in π^0 decays. The c_s correction also accounts for a smaller background, from π^- mesons misidentified as electrons.

Dalitz decay of the π^0 ($\pi^0 \to \gamma e^+ e^-$) or Bethe-Heitler conversions of one of the photons from "normal" π^0 decay ($\pi^0 \to \gamma\gamma$) both produce electron-positron pairs. Because there are equal numbers of electrons and positrons produced from π^0 decays, the rate and asymmetry of positrons can be used to correct the electron sample. We therefore define $c_s = 1 + (N_{e^+}/N_{e^-})$. To compare the electron/positron rates within the same acceptance, with both particles in-bending or both particles out-bending, we use our data taken with opposite torus fields. The results, binned in momentum and polar angle (p, θ), are shown in Fig. 7, for the case where both electron and positron are in-bending (red), and where both are out-bending (green). The average of the two was used to evaluate c_s. It can be seen that the ratios are negligibly small for $P > 2$ GeV, independent of θ, but rise to very large values below $P = 1.2$ GeV. We therefore used the cut $P > 1.2$ GeV, corresponding to $y = \frac{\nu}{E} < 0.8$, in this analysis.

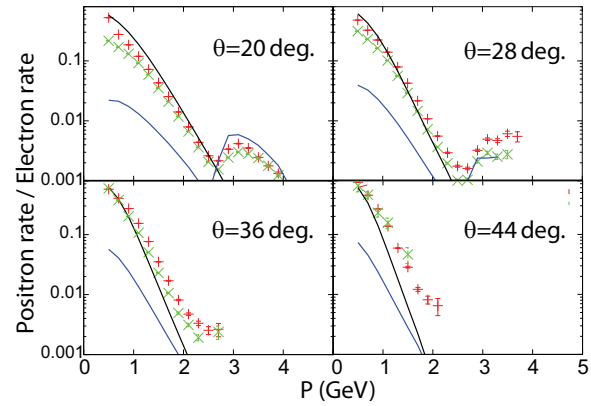

FIG. 7. (Color online) Ratio of positron to electron inclusive rates ($c_s - 1$) as a function of momentum for four bins in polar scattering angle θ. The green points are for both particles out-bending in the torus and the red points are for both particles in-bending. The curves are from a simulation (see text for details).

The ratios of e^+/e^- are compared with simulations based on the known rates of pion yields with 6 GeV electron beams [18]. The black curves are from π^0 decays, while the blue curves are from misidentified π^-. The simulation accounts quite well for the magnitude and kinematic dependence of the observed ratios. The enhancement seen above 2.65 GeV is a consequence of this value being the threshold for charged pions to produce light in the gas Cherenkov counter.

The functional form of the c_s correction (basically a dilution factor), arises from the assumption that the double-spin asymmetry for inclusive pion production is zero. Our measurements of positron asymmetries were found to be consistent with this assumption, when the positron asymmetry is at least one order of magnitude smaller than the electron asymmetry.

K. Polarized nitrogen contribution

The c_1 term in Eq. (5) accounts for the polarized nitrogen contribution to the measured double-spin asymmetry. From the definition of the raw asymmetry in terms of the physics asymmetries of each of the polarizable nuclei in a target, it is straightforward to show that

$$c_1 = \frac{\eta_N}{\eta_{p,d}} \frac{A_N \sigma_N}{A_{p,d} \sigma_{p,d}} \frac{P_N}{P_{p,d}}, \tag{13}$$

where η is the number of nuclei of a given species, σ is the cross section per nucleus, A is the double-spin asymmetry (hence $A\sigma$ is the cross-section difference), and P is the polarization of a given material. For each of these four variables, the subscript N is for nitrogen-14, and (p,d) refers to either the proton (for the NH_3 target) or deuteron (for the ND_3 target). The first term $(\eta_N/\eta_{p,d})$ in Eq. (13) is 1/3, by definition, for ammonia.

In the nuclear shell model, the spin-1 nitrogen-14 nucleus can be considered as a spinless carbon nucleus surrounded by an extra proton and neutron, each in a $1p_{\frac{1}{2}}$ orbital state [19]. After doing the spin projections, it turns out that the proton and neutron are each twice as likely to have their spin antialigned with the nitrogen spin, as having it aligned. It then follows that the second factor in Eq. (13) can be evaluated using

$$A_N\sigma_N = -\tfrac{1}{3}(\sigma_p A_p + \sigma_n A_n) = -\tfrac{1}{3}\sigma_d A_d, \qquad (14)$$

where the subscript n refers to the neutron, and we have neglected the small d-state correction and used the relation $\sigma_d = \sigma_p + \sigma_n$. Inserting this into the second term of Eq. (13), we obtain a constant value of -0.33 ± 0.08 for the ND_3 target and $(-0.33 \pm 0.08)A_d/A_p$ for the NH_3 target. The uncertainty of 0.08 comes from an evaluation [20] of a range of more sophisticated treatments of the nitrogen wave function than the simple shell model.

The third factor, the ratio of nitrogen to proton (deuteron) polarizations, can be evaluated using equal spin temperature (EST) theory [20,21]. This gives $P_N/P_p = 0.098$ for the average value $P_p = 0.77$ of this experiment. Experimental measurements from the SMC [20] are consistent with this result, although about 10%–15% higher. We therefore used $P_N/P_p = 0.10 \pm 0.01$. The EST theory predicts $P_N/P_d = 0.48$, essentially independent of P_d. An experimental study at SLAC (E143 experiment, unpublished) yielded a much lower value of $P_N/P_d = 0.33$. We therefore used an average: $P_N/P_d = 0.40 \pm 0.08$.

Combining all these results together yields:

$$c_1^p = (-0.011 \pm 0.003)(\sigma_d/\sigma_p)(A_d/A_p), \qquad (15)$$

$$c_1^d = -0.044 \pm 0.014. \qquad (16)$$

To evaluate σ_d/σ_p, the ratio of deuteron to proton cross section per nucleus, we used recent fits to world data [22,23]. To evaluate the ratio of double-spin asymmetries A_d/A_p we used an empirical fit to previous world data [24].

The values of c_1^p vary between -0.007 at low x and -0.013 at high x, with little dependence on Q^2.

L. Correction for NH_3 in ND_3

The c_2 term in Eq. (6) accounts for the polarized NH_3 contribution to the measured double-spin asymmetry in the nominal ND_3 target. As discussed above, the ND_3 target contained an approximately 10.5% (by weight) admixture of NH_3 (or equivalent), and the protons in this material were polarized. In the following treatment, we consider NH_3 as a background, and we define c_2 as

$$c_2 = \frac{\eta_p}{\eta_d}\frac{P_p}{P_d}, \qquad (17)$$

where the variables have the same meaning as in Eq. (13). The derivation of Eq. (17) is valid only if the dilution factor f in Eq. (6) is defined using the number of polarizable nucleons in deuterium only (not including the free protons), in the numerator of the ratio.

From the discussion above, the ratio of proton to deuteron nuclei is 0.105 ± 0.004 (0.120 ± 0.006) for the in-bending (out-bending) portion of Part C. The ratio of proton to deuteron polarizations is 2.31 ± 0.2 (2.15 ± 0.3) for the in-bending (out-bending) portion of Part C. Numerically, we then obtain for the average values:

$$c_2 = (0.24 \pm 0.02) \quad \text{in-bending}, \qquad (18)$$

$$c_2 = (0.26 \pm 0.04) \quad \text{out-bending}. \qquad (19)$$

M. Radiative corrections

In our analysis we approximate the scattering process as a one-photon exchange process, also called Born scattering. The higher order processes contributing to the total measured cross sections and asymmetries are taken into account by calculating radiative corrections. The radiative corrections can be broken into two kinds: internal and external. The internal processes occur within the field of the scattering nucleus and consist of the vertex corrections [which effectively account for the running of the fine coupling "constant" $\alpha(Q^2)$], as well as the emission of hard photons from the incident or scattered electron. External radiation occurs when a Bremsstrahlung photon is emitted from the incident electron prior to scattering (from a different nucleus from which the hard scattering takes place), or a hard photon is radiated by the scattered electron. The probability of emitting a hard photon is approximately given by tdk/k, where t is the material thickness in radiation lengths, and k is the photon energy. An important consideration is that an electron is de-polarized by the emission of Bremsstrahlung photons. As a rough guide at JLab energies, internal radiation is equivalent to external radiation when t is on the order a few percent. The main difference between the two is that the electron angles are essentially unchanged in external radiation (characteristic angle m_e/E), whereas significant changes in the electron scattering at the vertex can occasionally occur in the internal radiation process. For our ammonia targets, the values of t relevant for external radiation are about 1.2% for the incident electron and 4% for the scattered electron.

The radiative corrections require the evaluation of both polarized and unpolarized components for Born, internally radiated, and fully radiated cross sections and asymmetries. Polarization-dependent internal radiative cross sections were calculated using the formalism developed by Kuchto and Shumeiko [2,25]. External radiation was taken into account by convoluting internal radiative corrections with the spectrum of incident electron energies, rather than a single monochromatic value, according to the formalism of Mo and Tsai [26]. The external radiation from the scattered electron was similarly taken into account.

The calculations were done with the computer code RCSLACPOL, developed for the E143 experiment at SLAC in the early 1990s [2]. The code requires input models for inelastic electron scattering as well as ep elastic (proton target) or ep and en quasielastic scattering. For spin-averaged inelastic cross sections, we used the recent fits to world data of Christy and Bosted [22] for the proton and Bosted and Christy [23] for the deuteron. Spin-dependent inelastic cross sections were obtained using a recent fit to JLab data [27].

In our correction scheme, the radiative corrections are broken into an additive correction $A_{\rm RC}$, and a radiative dilution factor $f_{\rm RC}$. The factor $f_{\rm RC}$ is nothing more than $(1 - f_e)$, where f_e is the fraction of events that have radiated down into a given (x, Q^2) bin from the ep elastic scattering process (or quasielastic process for the deuteron target). The factor $A_{\rm RC}$ accounts for all other radiative processes. The radiatively corrected asymmetry is then given by

$$A_{\rm corr} = A_{\rm uncorr}/f_{\rm RC} - A_{\rm RC}. \tag{20}$$

The statistical uncertainty on the corrected asymmetry is given by

$$\delta A_{\rm corr} = \delta A_{\rm uncorr}/f_{\rm RC}. \tag{21}$$

The corrections were found to be very small for $y = \frac{\nu}{E} < 0.8$, the cut used in this analysis, corresponding to typical changes in g_1/F_1 of less than 1%. The largest effects are in the resonance region, where the asymmetry is changing rapidly with W. The error bars with radiative corrections applied are larger than without corrections, with the biggest increase at the largest W of a given Q^2 bin (corresponding to large values of y). The effect of radiative corrections for the deuteron is even smaller than for the proton.

IV. RESULTS AND COMPARISON TO THEORY

A. Results for g_1/F_1

In the one-photon-exchange (Born) approximation, the cross section for inclusive electron scattering with beam and target spin parallel ($\uparrow\Uparrow$) or antiparallel ($\uparrow\Downarrow$) can be expressed in terms of the four structure functions F_1, F_2, g_1, and g_2, all of which can depend on ν and Q^2 [24]:

$$\frac{d\sigma^{\uparrow\Downarrow/\uparrow\Uparrow}}{d\Omega dE'} = \sigma_M \left[\frac{F_2}{\nu} + 2\tan^2\frac{\theta}{2}\frac{F_1}{M} \pm 2\tan^2\frac{\theta}{2} \times \left(\frac{E_0 + E'\cos\theta}{M\nu} g_1 - \frac{Q^2}{M\nu^2} g_2 \right) \right], \tag{22}$$

where the Mott cross section,

$$\sigma_M = \frac{4E'^2\alpha^2\cos^2\frac{\theta}{2}}{Q^4}. \tag{23}$$

We can now define the double-spin asymmetry $A_\parallel$ as

$$A_\parallel(\nu, Q^2, y) = \frac{d\sigma^{\uparrow\Downarrow} - d\sigma^{\uparrow\Uparrow}}{d\sigma^{\uparrow\Downarrow} + d\sigma^{\uparrow\Uparrow}}. \tag{24}$$

The measured asymmetry $A_\parallel$ contains contributions from both the g_1 and g_2 structure functions. After some algebra, the equations can be rewritten as

$$g_1/F_1 = (A_\parallel/D')C_{g_2}, \tag{25}$$

where the depolarization factor in this case is given by [2]

$$D' = \frac{(1-\epsilon)(2-y)}{y(1+\epsilon R)}, \tag{26}$$

with $\epsilon = (1 + 2(1+\tau)(\tan(\frac{\theta}{2}))^2)^{-1}$ and $\tau = \frac{\nu^2}{Q^2}$. The ratio R of longitudinal to transverse virtual photon absorption cross section is

$$R = \frac{\sigma_L(\gamma^*)}{\sigma_T(\gamma^*)} = \frac{F_2}{2xF_1}(1+\gamma^2) - 1, \tag{27}$$

where $\gamma = \frac{\sqrt{Q^2}}{\nu}$. The correction factor due to g_2, C_{g_2} is described in the section below.

1. Depolarization factor and R

This depolarization factor is a function of R [Eq. (27)], which we obtained from a fit to world data [22]. The fit describes the range $0 \leqslant Q^2 \leqslant 8$ GeV^2 and $1.1 \leqslant W \leqslant 3.1$ GeV which covers the area of interest for this study. Typical values of R vary between 0.1 and 0.3 for both the proton and the deuteron, with a typical uncertainty of 0.03.

2. g_2 correction

The g_2 correction factor is given by

$$C_{g_2} = \frac{1 + E'/E_0}{1 + E'\cos(\theta)/E_0} \frac{1}{1 - 2(g_2/g_1)Mx/[E_0 + E'\cos(\theta)]}. \tag{28}$$

To gauge the rough order of magnitude of the correction, we note that for $\cos(\theta) = 1$, $x = 0.5$, $E_0 = 6$ GeV, then

$$C_{g_2} \approx 1 + (g_2/g_1)/10. \tag{29}$$

Because g_2 is smaller in magnitude than g_1, the overall correction differs by only a few percent from unity, as illustrated in Fig. 8.

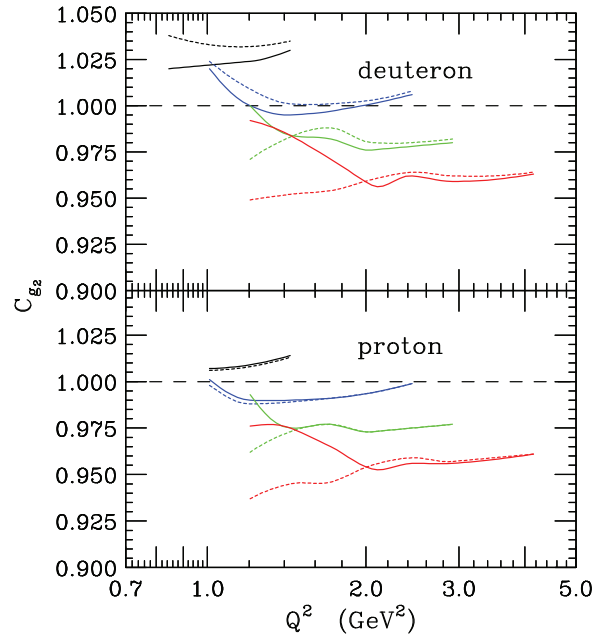

FIG. 8. (Color online) Correction factor C_{g_2} as a function of Q^2. The curves are, from top to bottom, $x = 0.225$ (black), $x = 0.325$ (blue), $x = 0.425$ (green), and $x = 0.525$ (red). Lower panel is for the proton target, upper panel for the deuteron. Dashed curves use the lowest-twist Wandzura and Wilczeck formula, while the solid curves use a fit to world data.

TABLE IV. Summary of relative systematic uncertainties in $A_\parallel$ for proton and deuteron.

Factor	Proton	Deuteron
f	2.3%	2.3%
$P_b P_t$	1.4%	7.0%
c_s	0%–3%	0%–3%
c_1	0.3%	1.4%
c_2	n/a	5%–10%
R.C.	0.5%	0.5%
r_c	0.1%	0.1%
Total	2.8%–4.1%	8.1%–12%

The values of g_2/g_1 used in the analysis were taken from a fit to world data [27]. To estimate the systematic uncertainty on the correction, we also used the assumption that there are no deviations from the twist-two model of Wandzura and Wilczeck (g_2^{WW}) [28], in which

$$g_2(x,Q^2) = -g_1(x,Q^2) + \int_x^1 g_1(\xi,Q^2)d\xi/\xi. \qquad (30)$$

In this relation, the magnitude of g_1 cancels, and the result depends only on the x dependence at higher x. The corrections C_{g_2} using only the Wandzura and Wilczeck contribution are shown as the dashed curves in Fig. 8. The differences from the world fit of Ref. [27] are quite small, except for $x = 0.525$ at low Q^2.

3. *Combining data sets*

Physics quantities that should depend only on (x, Q^2) [or equivalently (W, Q^2)] were first calculated for each beam energy and torus polarity. These physics quantities were then combined, weighted by their statistical uncertainties. The proton results used only Parts A and B, due to the very small amount of proton data in Part C. The deuteron data are from Part C only. Data from each of the individual run periods were compared with the corresponding averages, and found to be consistent within overall normalization uncertainties (dominated by the uncertainty in $P_b P_t$).

B. Systematic uncertainties

In this section we first summarize the systematic uncertainties on $A_\parallel$ arising from each of the terms in Eqs. (5) and (6).

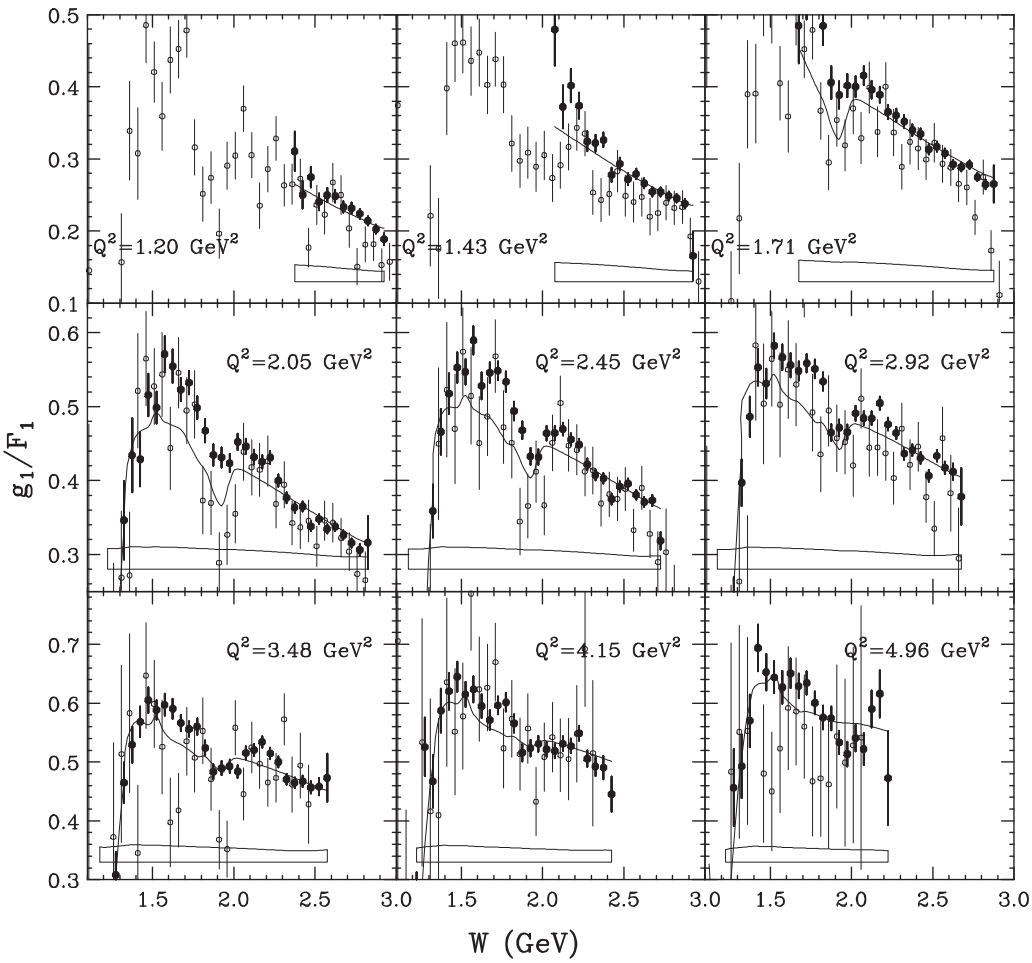

FIG. 9. Results for g_1/F_1 as a function of W for the proton in nine bins of Q^2. The present results are shown as solid circles, and the published Eg1b results are shown as open circles.

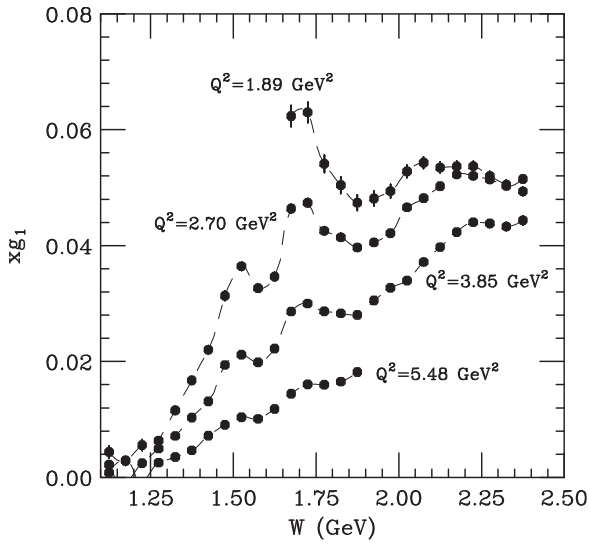

FIG. 10. Results for xg_1 as a function of W for the proton in four bins of Q^2. The dashed lines simply connect the results at a particular value of Q^2.

We then discuss the systematic uncertainties from three other additional sources, which were assumed to be negligible in these equations.

1. Beam charge ratio r_c

The uncertainty in the ratio of incident beam charge for positive and negative helicities (relative to the target polarization direction) was much less than 0.0001 on a few-minute time scale. This negligibly small value was achieved by three methods: (1) frequent reversal of the half-wave plate in the CEBAF injector; (2) keeping the charge asymmetry less than 0.1% using an on-line feedback system; and (3) generating beam helicity buckets in pairs.

2. Dilution factor f

The dilution factor is one of the two most important sources of systematic uncertainties in the determination of $A_\parallel$. There are several factors which contribute here:

(1) The ammonia length l_A has an estimated relative uncertainty of 3% for most of the experiment, based on the spread in the individual determinations for pairs of carbon and ammonia runs, combined with an overall uncertainty of 1% in the carbon target areal density.
(2) The length of the He bath L (which determines how much helium there is in the target), has an estimated uncertainty of 0.2 cm, based on inconsistencies between the determination of 2.0 cm from the empty target runs, and 2.3 cm for a direct measurement in the laboratory when the target was at room temperature.
(3) The areal density of the aluminum He containment windows has an estimated uncertainty of 0.005 g/cm^2 (a relative uncertainty of 10%).
(4) The areal density of the target Kapton windows has an estimated uncertainty of 0.005 g/cm^2 (a relative uncertainty of 5%).
(5) Approximately 3% uncertainties in the density of ammonia and helium at 1 K.

Folding together these uncertainties for our particular target (i.e., about 70% ammonia by areal density, 30% other nuclei), the result is a 1.5% relative uncertainty in f, with no significant (x, Q^2) dependence for $W > 1.4$ GeV.

Although all of the above contributions vanish in the limit of a pure ammonia target, there is still the overall scale uncertainty in the ratios of spin-averaged inclusive cross sections σ_p/σ_{14N} and σ_d/σ_{14N}. Based on the fluctuations between various experiments fit in Refs. [15,22,23], we estimate the uncertainties be 1.5% in both cases. Combining this with the target-parameter-dependent uncertainty of 1.5%, the total relative uncertainty in f is 2.3% for both proton and deuteron.

3. Product of beam and target polarization $P_B P_T$

For the proton, the relative uncertainty on $P_b P_t$ has a statistical component of 1% (averaged over Parts A and B). We estimate a further systematic uncertainty of 1% coming from the choice of cuts and the model for G_E/G_M. The net systematic uncertainty on $P_b P_t$ for the proton is therefore 1.4%.

For the deuteron, we estimate an overall normalization uncertainty of 3% to 5% in the target polarization values extracted from the NMR signals by the double-peak method. The systematic uncertainty on the beam polarization from the Møller methods is estimated to be 4%, based on comparison with more accurate measurements made in Halls A and C over a period of many years. The net result is an overall relative systematic uncertainty of 7% in $P_b P_t$ for the deuteron.

4. Uncertainty associated with pair-symmetric and misidentified pion correction

The correction term, $c_s - 1$, is negligibly small for $P > 2$ GeV ($y < 0.65$), but rises to values as large as $c_s - 1 = 0.10$ at $P = 1.2$ ($y = 0.8$), the lowest value of P used in the analysis. Based on the disagreement between our two measurements (both particles in-bending, or both out-bending), we assigned a systematic uncertainty of 30% on $c_s - 1$, corresponding to a systematic uncertainty of up to 3% on $A_\parallel$ at the highest values of y.

We assumed that the pair-symmetric asymmetry was zero, however, at low P, there are some indications that the scaled contribution could be as large as 1% for $1.2 < P < 1.5$ GeV for the proton, and as much as 3% for the deuteron. We therefore assigned a relative systematic uncertainty of 1% (3%) to $A_\parallel$ for the proton (deuteron) for $P < 1.5$ GeV.

5. Uncertainty associated with radiative corrections

The application of radiative corrections make typically less than 1% changes to g_1/F_1. To study the systematic uncertainty, radiative corrections were calculated with several alternate cross section and asymmetry models. No significant changes were observed, at the 0.5% level.

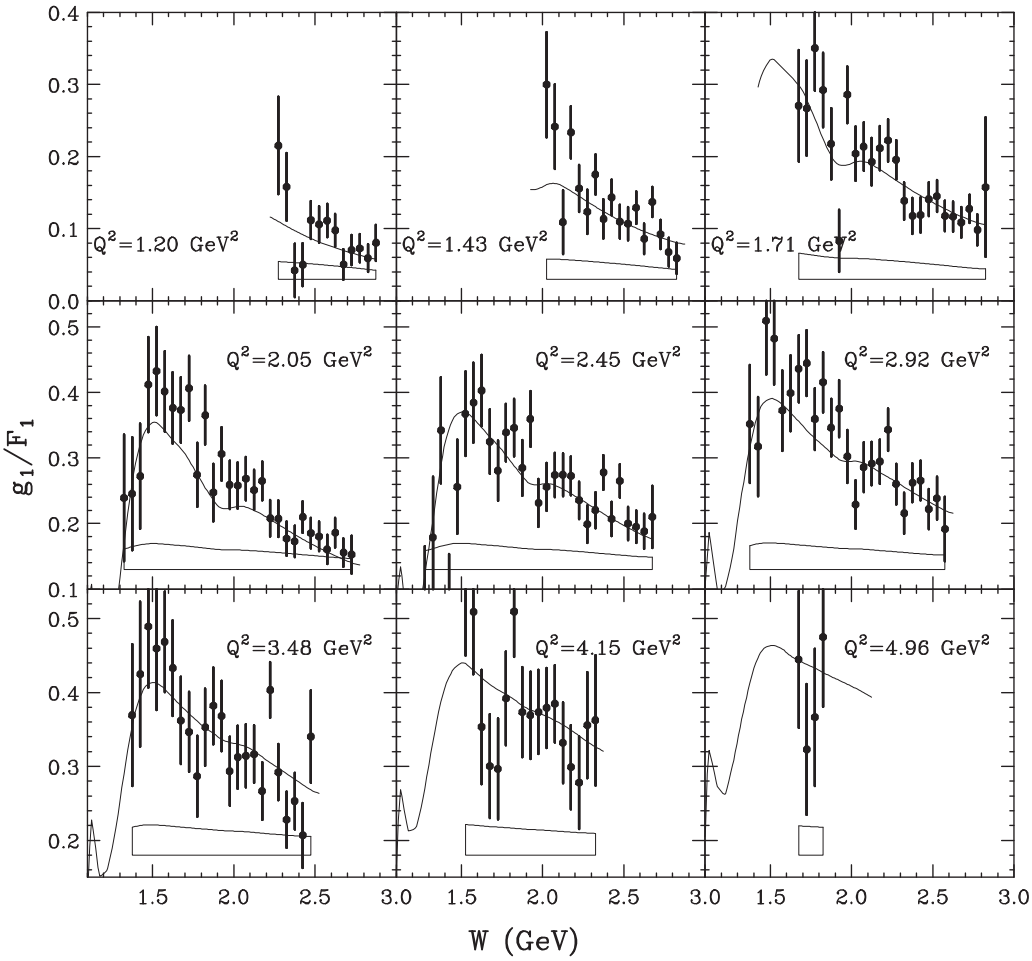

FIG. 11. Same as Fig. 9 except for the deuteron. For clarity, data from Eg1b are not shown.

6. *Uncertainty on c_1*

The uncertainty on the value of c_1 was estimated to be 0.003 (0.014) for the proton (deuteron), independent of (x, Q^2), based on the uncertainties in modeling nitrogen-14, as discussed in Sec. III K.

7. *Uncertainty on c_2*

The uncertainty on the value of c_2 was estimated to be 0.025 (0.038) for the in-bending (out-bending) deuteron asymmetries, independent of (x, Q^2). The corresponding relative uncertainty in the deuteron asymmetries and structure functions is given by $0.025 A_\parallel^p / A_\parallel^d$ for the in-bending runs, and $0.038 A_\parallel^p / A_\parallel^d$ for the out-bending runs, where the ratio $A_\parallel^p / A_\parallel^d$ varies between 2 and 3 over the (x, Q^2) range of the experiment.

8. *Detection efficiency*

In Eqs. (5) and (6), we assumed that the detector efficiency was the same for target and beam polarization aligned or antialigned. A correction should be made if the overall particle rate is higher for one state than the other, resulting in a rate dependence to the detection efficiency. We estimated that if the total particle rate were entirely good electrons, the measured asymmetry would be 7% lower than if the detector efficiency were not rate dependent. Fortunately, the total particle rate was dominated (>95%) by photo-produced pions, rather than scattered electrons.

From measurements at SLAC [29], we know that the raw asymmetry in pion production is an order of magnitude smaller than for electron scattering. Therefore the correction would be on the order of 0.7%. Taking into account that approximately the same correction applies to ep elastic scattering (from which we determine $P_B P_T$), the net effect on the final electron asymmetry is reduced even further. We therefore made no correction for rate-dependent detection efficiency, and assign an overall systematic uncertainty of 0.7%.

9. *Parity-violating background*

The raw asymmetry arising due to eN parity-violating inelastic scattering from any of the nucleons in the target is given to a good approximation by $A_\parallel^{PV} = P_b Q^2 [0.8 \times 10^{-4}]$, independent of x (from the Particle Data Book [30]). Because $A_\parallel^{\mathrm{PV}}$ does not depend on target polarization P_T (unlike the double-spin asymmetry $A_\parallel$), the contribution to $A_\parallel$ cancels, by definition, for equal running times with the target polarization aligned (denoted by t^+) or antialigned (t^-) with the beam direction. For unequal running times, the contribution

from $A_\parallel^{\rm PV}$ is reduced by a factor $r_T = (t^+ - t^-)/(t^+ + t^-)$. Averaged over the entire experiment, $r_T = 0.04$ for NH_3 and $r_T = 0.11$ for ND_3. Because the measured raw double-spin raw asymmetry is approximately given by $Q^2 \times 10^{-2}$ for our average virtual photon energy $\nu = 3$ GeV, the relative parity-violating contribution was less than 0.1% in all (x, Q^2) bins, and was neglected.

10. Summary of systematic uncertainties on $A_\parallel$

With all of the above uncertainties added in quadrature, the overall relative systematic uncertainty on $A_\parallel$ has an (x, Q^2)-independent value of 2.8% for the proton and 8.1% for the deuteron. The proton uncertainty is dominated by the uncertainty in f, while the deuteron is dominated by the uncertainty in $P_b P_t$. The only systematic uncertainty that depends strongly on kinematic values for the proton is the pair-symmetric correction, which increases the overall uncertainty to 4.1% (8.6%) for the proton (deuteron) at $y = 0.8$. For the deuteron, the c_2 contribution varies significantly with kinematics also. A summary of systematic uncertainty factors contributing to $\Delta A_\parallel$ is presented in Table IV.

C. Systematic uncertainty on g_1/F_1

Equation (25) shows that the systematic uncertainty on g_1/F_1 has two additional sources compared to $A_\parallel$: the uncertainty on D' (dominated by the uncertainty in R), and the uncertainty on the g_2 correction. Because the knowledge of R and g_2 may improve in the future, we list the values we used in the final results table.

1. Uncertainty on D'

The dominant uncertainty in D' comes from the uncertainty in R (because $\frac{dD'}{D'} = \epsilon dR$). Fortunately, relatively recent precision data from JLab have reduced the overall uncertainty in R in the kinematic region of the present experiment to approximately 0.03 (see Ref. [22]). Because $0.4 < \epsilon < 0.9$ for the present experiment, the uncertainty in R introduces a relative uncertainty of 1% to 3% in g_1/F_1. Another source of uncertainty in D' comes from the estimated systematic uncertainties in the beam energy of 10 MeV, the electron momentum P of about $0.002P$, and the scattering angle θ of about 0.5 mr. Taken together, these result in a relative uncertainty in D' of 0.5%–1%, with the largest uncertainty at large y.

2. Uncertainty on the g_2 correction

The values of g_2/g_1 used in the analysis were taken from a fit to world data [27]. To estimate the systematic uncertainty on the correction, we also used the assumption that there are no deviations from the twist-two model of Wandzura and Wilczeck (g_2^{WW}) [28]. We estimated the systematic uncertainty on the g_2 correction to be about ~3% for both targets.

D. Physics results

The essential physics results from this analysis are the ratios g_1/F_1 for the proton and deuteron, from which g_1 can be obtained by using fits of world data of F_1. These results can be examined as a function of W to look for resonance structure, and as a function of x to study quark and gluon spin distributions, taking into account higher-twist contributions.

1. g_1/F_1 as a function of W

The results for g_1/F_1 as a function of W are shown for the proton in nine bins of Q^2 in Fig. 9.

The systematic uncertainty bands are dominated by an overall normalization uncertainty common to all points. The results are in reasonable agreement with the published results from the Eg1b experiment [6], but have typically five times higher statistical precision, and a factor of two better systematic precision. The Eg1b results are on average a few percent lower than the present results, which is well within the overall systematic uncertainty of the two experiments (about 3% for this experiment and 7% for Eg1b).

The bands at the bottom of each panel represent the total systematic uncertainty (point to point as well as overall normalization uncertainties combined). Note the offset from 0 in the vertical axis of most of the panels.

These higher precision results for g_1/F_1 clearly show some resonantlike structure for values of W as high as 2.4 GeV. To see the higher-W structures more clearly, we plot xg_1 in Fig. 10. In this plot, pairs of adjacent Q^2 bins have been averaged together.

The downward trend seen in the g_1/F_1 plot, near $W = 1.23$ GeV, can be attributed to transitions to the spin-3/2 $\Delta(1232)$. The dip can be understood by realizing that g_1/F_1 is closely related to

$$A_1 = \frac{\sigma_{1/2} - \sigma_{3/2}}{\sigma_{1/2} + \sigma_{3/2}}, \tag{31}$$

where $\sigma_{1/2}$ ($\sigma_{3/2}$) represent transitions to final state helicity 1/2(3/2). For a pure $N \to \Delta$ transition, $A_1 = -0.5$.

The strong peak near 1.5 GeV seen in both the g_1/F_1 and the xg_1 plots is dominated by transitions to two nucleon resonances, the $N(1520)$ $3/2^-$ and $N(1535)$ $1/2^-$ states. The spin-1/2 $N(1535)$ resonance has only helicity = 1/2 transition amplitudes contributing, while the spin-3/2 $N(1520)$ state has contributions from both helicity = 1/2 and helicity = 3/2 transition amplitudes, and therefore can exhibit a range of asymmetry values, from $A_1 = -1$ for $\sigma_{3/2}$ dominance to $A_1 = +1$ for $\sigma_{1/2}$ dominance. As was found in the analysis of single pion (π) and single eta (η) exclusive cross-section measurements from other CLAS experiments [31,32], the helicity structure of this state changes rapidly from $A_1 = -1$ at $Q^2 = 0\,\text{GeV}^2$ to $A_1 = +1$ at $Q^2 > 1\,\text{GeV}^2$. In the Q^2 range of this experiment both states have $A_1 = +1$ to create the strong peak at 1.5 GeV.

The peak near 1.7 GeV has a similar origin. While more resonances contribute in this mass range, the $N(1680)$ $5/2^+$ state was found to be by far the most dominant one for a proton target. The helicity structure is similar to the $N(1520)$ $3/2^-$ discussed above, and shows a dominant helicity 3/2 transition at $Q^2 = 0\,\text{GeV}^2$, which changes to helicity 1/2 dominance for $Q^2 > 1\,\text{GeV}^2$, resulting in asymmetry $A_1 > 0$, growing with Q^2. All of these features have been seen before, at somewhat

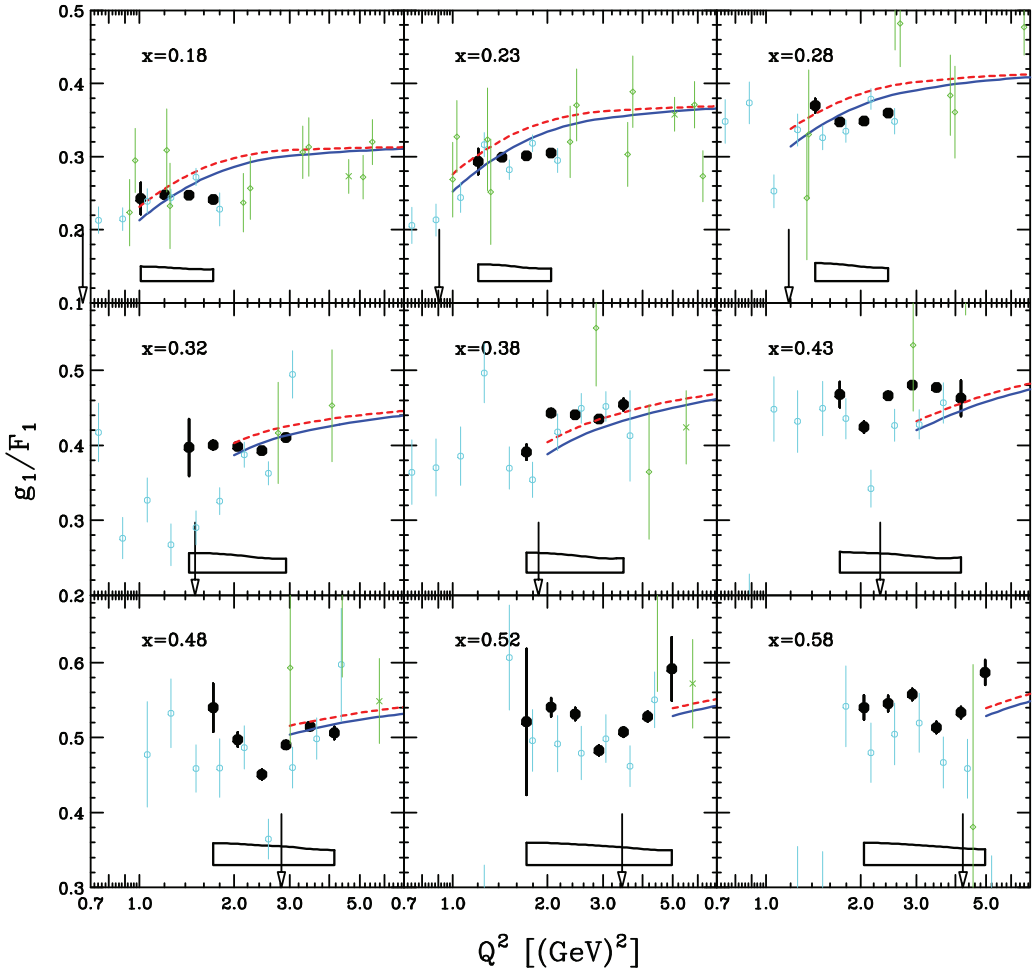

FIG. 12. (Color online) Results for g_1/F_1 as a function of Q^2 for the proton in nine bins of x. A bin centering correction was applied to the data points in this plot, of the form $\frac{g_1}{F_1}(x_c, Q^2)/\frac{g_1}{F_1}(x, Q^2)$, where x_c is the value of x at the center of the bin, and x and Q^2 are the experimental averages over the size of the bin. The present results are shown as the large black solid points, the JLab Eg1b results [6] are shown as the small blue points, and the results from SLAC [2,3] are shown as the small green points. The arrows correspond to $W = 2$ GeV.

lower Q^2 [6,33]. What is interesting is that all three primary resonance regions are visible for Q^2 values as high as 4 GeV^2.

What is new in the present results is a confirmation of an apparent dip near $W = 1.9$ GeV, with a possible peak near $W = 2.2$ GeV (sometimes known as the fourth resonance region). Hints of these structures were seen in the Eg1b results [6]. The strength of the dip near $W = 1.9$ GeV seems to decrease with increasing Q^2. This could indicate significant contributions from resonances with dominant helicity $= 3/2$ transitions. There is a number of states in this mass range that could contribute to the observed structure.

To investigate this possibility further, we are in the process of analyzing exclusive single pion (π) and eta (η) electroproduction from the same experiment. The analysis of pion production on neutrons may provide information on the isospin of the resonance contribution.

The results for g_1/F_1 for the deuteron are shown in Fig. 11. The comparison to the world data fit (dominated by Eg1b results [6]) is reasonably good. The structure seen in the proton results is not as pronounced, largely due to the factor of six to eight larger error bars, resulting from 1/3 of the integrated luminosity, a factor of almost three lower $P_b P_t$, and the NH_3 contamination of the target.

2. *Results for g_1/F_1 as a function of Q^2*

The results for g_1/F_1 as a function of Q^2 are shown for the proton in nine bins of x in Fig. 12. The systematic uncertainty bands are dominated by an overall normalization uncertainty common to all points. Small bin-centering corrections have been applied to the data: Typically these are only significant in the highest and lowest Q^2 bins in each panel.

The bands at the bottom of each panel represent the total systematic uncertainty (with point-to-point and overall normalization uncertainties combined). The dashed red and solid blue curves are representative pQCD calculation from the LSS group with two models for gluon polarization [34].

The results for the deuteron are shown in Fig. 13. These data are in good agreement with Eg1b [6] SLAC [2,3], COMPASS [4], and HERMES [5]. The data are also reasonably consistent with the fit used for radiative and other corrections (black curves) as well as the two pQCD calculations from LSS

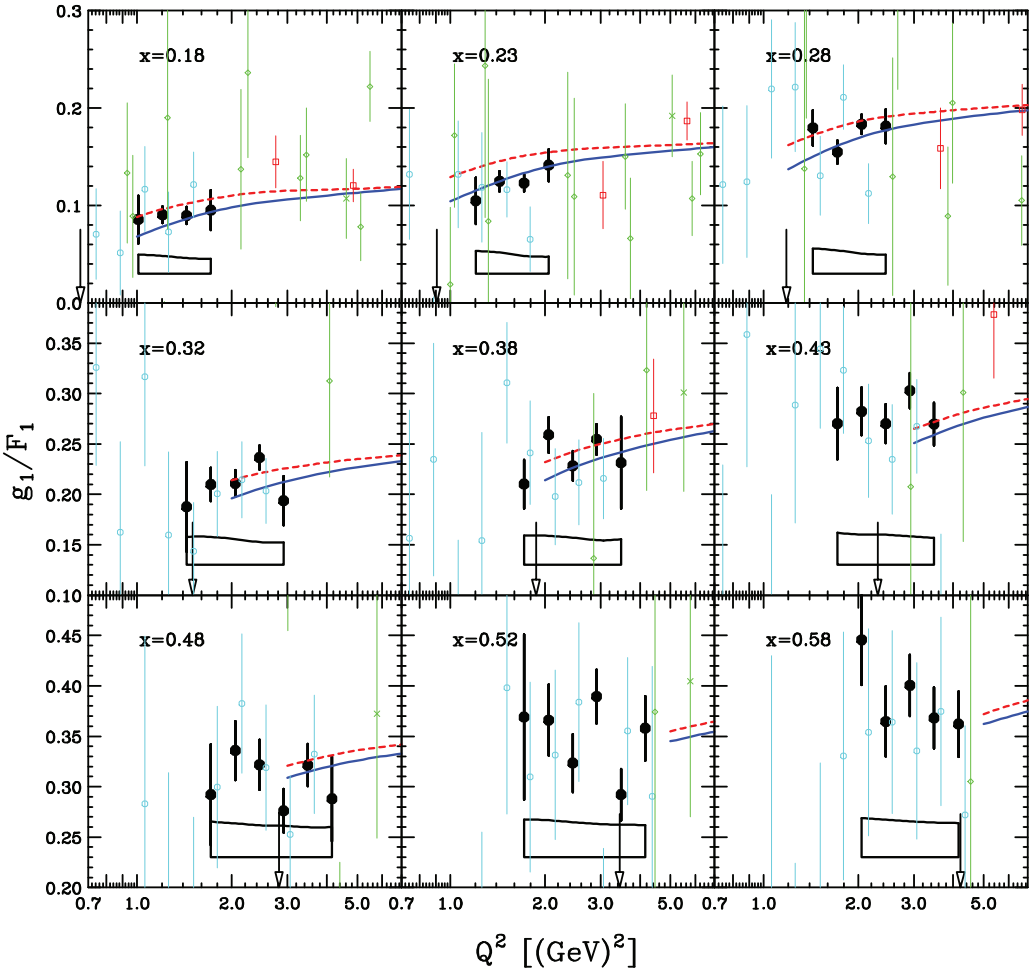

FIG. 13. (Color online) Same as Fig. 12 except for the deuteron. The small green points include results from COMPASS [4], HERMES [5], and SLAC [2,3]. A bin centering correction was applied to the data points in this plot, of the form $\frac{g_1}{F_1}(x_c, Q^2)/\frac{g_1}{F_1}(x, Q^2)$, where x_c is the value of x at the center of the bin, and x and Q^2 are the experimental averages over the size of the bin.

[34]. As for the proton case, the deuteron data show less Q^2 dependence than either model, and are completely consistent with no Q^2 dependence at all for $W > 2$ GeV.

The data are consistent with previous CLAS data with 6 GeV electrons [6] (blue points), and higher beam energy data from SLAC [2,3], shown as the green points. In the region of overlap, the present data have much higher statistical and systematic precision, allowing for a detailed study of the Q^2 dependence of g_1/F_1 at fixed x.

The blue and red curves are pQCD calculations from the LSS group [34] with positive ΔG (blue curves) and negative ΔG (red curves). In each case, higher twist coefficients were fit to give the best agreement with the data available in 2007. The difference in overall magnitude between the curves is of the same order or larger than our experimental error bars. However, the Q^2 dependence is generally larger than in the data, and the magnitude of the curves is above the data at low x and below at higher x. It appears that the curves with negative ΔG agree better with the flat Q^2 dependence of our data than the positive ΔG curves. Any such conclusions must be treated with great caution, because the data clearly show oscillations around a smooth curve, with a dip seen just below the Q^2 values corresponding to $W = 2$ GeV, shown as the arrows in the figure panels.

V. CONCLUSION

We have made the most precise measurements to date of g_1^p and g_1^d, in the kinematic range available with a 6 GeV lepton beam. Examined as a function of W, the results show resonant structure in the three well-known resonance regions ($W = 1.2$, 1.5, and 1.7 GeV), as well as a possible peak near 2.2 GeV, with a dip near 1.9 GeV. This is the first time some of these resonant structures are clearly seen at Q^2 values well above 1 GeV^2.

Examined in the variables (x, Q^2), the most striking result is the almost complete lack of any significant Q^2 dependence in the ratio g_1/F_1 for $W > 2.2$ GeV and $0.15 < x < 0.5$. On the other hand, significant oscillations around a smooth curve are observed at values of (x, Q^2) corresponding to $W < 2.2$ GeV.

A new global pQCD fit that includes our new data should be able to significantly improve the determination of higher twist corrections. In addition, these data will provide more available

input to the global pQCD fits which can be used to put new constraints on ΔG.

Such a fit will need to take into account the effects of nucleon resonance structure below W of approximately 2.4 GeV. Options include simply placing a cut $W > 2.4$ GeV, using higher-twist forms that take nucleon resonance structure into accounts, or smoothing over resonance structure in some fashion, such as by invoking quark-hadron duality in the spin structure functions [35].

The availability of an 11 GeV electron beam at Jefferson Lab, coupled with a new CLAS12 detector, will soon permit measurements of g_1 at higher values of W with good statistical precision. These data will be crucial for advancing our knowledge of the spin structure of the nucleon.

ACKNOWLEDGMENTS

We would like to acknowledge the outstanding efforts of the staff of the Accelerator and the Physics Divisions at Jefferson Lab that made this experiment possible. This work was supported in part by the U.S. Department of Energy and the National Science Foundation, the Italian Instituto Nazionale di Fisica Nucleare, the French Centre National de la Recherche Scientifique, the French Commissariat à l'Energie Atomique, the United Kingdom's Science and Technology Facilities Council, the Chilean CONICYT, and the National Research Foundation of Korea. The Southeastern Universities Research Association (SURA) operates the Thomas Jefferson National Accelerator Facility for the United States Department of Energy under Contract No. DE-AC05-06OR23177.

[1] C. Aidala, S. Bass, D. Hasch, and G. Mallot, Rev. Mod. Phys. **85**, 655 (2013).
[2] K. Abe *et al.* (SLAC E143 Collaboration), Phys. Rev. Lett. **74**, 346 (1995); **75**, 25 (1995); Phys. Lett. B **364**, 61 (1995); Phys. Rev. D **58**, 112003 (1998).
[3] P. L. Anthony *et al.* (SLAC E155 Collaboration), Phys. Lett. B **463**, 339 (1999).
[4] V. Y. Alexakhin *et al.* (COMPASS Collaboration), Phys. Lett. B **647**, 8 (2007); E. S. Ageev *et al.* (COMPASS Collaboration), *ibid.* **612**, 154 (2005).
[5] A. Airapetian *et al.* (HERMES Collaboration), Phys. Lett. B **442**, 484 (1998); K. Ackerstaff *et al.* (HERMES Collaboration), *ibid.* **404**, 383 (1997); A. Airapetian *et al.* (HERMES Collaboration), Phys. Rev. D **75**, 012007 (2007).
[6] K. V. Dharmawardane *et al.* (CLAS Collaboration), Phys. Lett. B **641**, 11 (2006); Y. Prok *et al.* (CLAS Collaboration), *ibid.* **672**, 12 (2009).
[7] A. Adare *et al.* Phys. Rev. Lett. **103**, 012003 (2009).
[8] V. N. Gribov and L. N. Lipatov, Sov. J. Nucl. Phys. **15**, 675 (1972); Yu. L. Dokshitzer, Sov. Phys. JETP **46**, 641 (1977); G. Altarelli and G. Parisi, Nucl. Phys. B **126**, 298 (1977).
[9] E. Leader, A. V. Sidorov, and D. B. Stamenov, Phys. Rev. D **75**, 074027 (2007).
[10] P. Jimenez-Delgado, A. Accardi, and W. Melnitchouk, Phys. Rev. D **89**, 034025 (2014).
[11] B. A. Mecking *et al.*, Nucl. Instr. Meth. **503**, 513 (2003).
[12] R. Fatemi *et al.* (CLAS Collaboration), Phys. Rev. Lett. **91**, 222002 (2003).
[13] C. D. Keith *et al.* Nucl. Instrum. Meth. **501**, 327 (2003).
[14] P. E. Bosted, N. Kvaltine, and Y. Prok, "Inclusive Polarized Structure Functions g_1^p and g_1^d from the eg1-DVCS Experiment," CLAS-NOTE-2013-010 [https://misportal.jlab.org/ul/Physics/Hall-B/clas/index.cfm].
[15] P. E. Bosted and V. Mamyan, arXiv:1203.2262.
[16] CLAS Physics Database [http://clasweb.jlab.org/physicsdb].
[17] C. M. Dulya, Nucl. Instrum. Meth. A **398**, 109 (1997).
[18] D. Wiser, Ph.D. thesis, University of Wisconsin, 1977.
[19] O. A. Rondon, Phys. Rev. C **60**, 035201 (1999).
[20] B. Adeva *et al.* (Spin Muon Collaboration), Nucl. Instrum. Meth. A **419**, 60 (1998).
[21] D. G. Crabb and W. Meyer, Annu. Rev. Nucl. Part. Sci. **47**, 67 (1997).
[22] M. E. Christy and P. E. Bosted, Phys. Rev. C **81**, 055213 (2010).
[23] P. E. Bosted and M. E. Christy, Phys. Rev. C **77**, 065206 (2008).
[24] R. G. Fersch *et al.* (CLAS Collaboration) (unpublished).
[25] T. V. Kuchto and N. M. Shumeiko, Nucl. Phys. B **219**, 412 (1983).
[26] L. W. Mo and Y. S. Tsai, Rev. Mod. Phys. **41**, 205 (1969).
[27] N. Guler and S. Kuhn *et al.* (unpublished).
[28] S. Wandzura and F. Wilczek, Phys. Lett. B **72**, 195 (1977).
[29] P. L. Anthony *et al.* (E155 Collaboration), Phys. Lett. B **458**, 536 (1999).
[30] Particle Data Group [http://pdg.lbl.gov].
[31] I. G. Aznauryan *et al.* (CLAS Collaboration), Phys. Rev. C **80**, 055203 (2009).
[32] I. G. Aznauryan and V. D. Burkert, Prog. Part. Nucl. Phys. **67**, 1 (2012).
[33] F. R. Wesselmann *et al.* (RSS Collaboration), Phys. Rev. Lett. **98**, 132003 (2007).
[34] E. Leader, A. V. Sidorov, and D. B. Stamenov, Phys. Rev. D **73**, 034023 (2006).
[35] P. E. Bosted *et al.* (CLAS Collaboration), Phys. Rev. C **75**, 035203 (2007).